JM PAPERS

Controlled inertial nano-cavitation above 100 MHz

Ulisses J. Gutiérrez-Hernández[1,†,‡], **Hendrik Reese**[2,‡], **Claus-Dieter Ohl**[2] and **Pedro A. Quinto-Su**[1]

[1]Instituto de Ciencias Nucleares, Universidad Nacional Autónoma de México, Apartado Postal 70-543, 04510 Cd. Mx., México

[2]Department for Soft Matter, Institute of Physics, Otto-von-Guericke-Universität Magdeburg, Universitätsplatz 2, 39106 Magdeburg, Germany

The maximum size and lifetime of an acoustically nucleated cavitation bubble is inversely proportional to the driving frequency and has achieved a limit of approximately 10 MHz. Smaller cavitation bubbles that are critical to microscopic applications require shorter lifetimes that correspond to higher oscillation frequencies. Here, we demonstrate that acoustic cavitation in the 100 MHz range and beyond can be achieved through wave propagation in a solid rather than in a liquid. The cavitation bubble is nucleated at a nano-sized fracture on a glass substrate, and its expansion is driven by a leaky Rayleigh wave, while the inertial collapse is induced by a trailing shock wave. As both waves travel at different velocities, the time interval between these two events is a function of the distance to the source. In this way, we demonstrate experimentally control of the lifetime of the bubbles in a range between 6 and 80 ns, corresponding to oscillation frequencies between 13 and 166 MHz. Our results agree with finite-volume fluid–structure interaction simulations.

Key words: shock waves, cavitation, elastic waves

1. Introduction

Acoustic cavitation refers to bubble generation in a liquid using acoustic waves. These bubbles have been used in various fields, e.g. medical research for drug delivery (Stride & Coussios 2019), cell and cell organelle surgery (Prentice *et al.* 2005; Chen *et al.* 2011), semiconductor cleaning (Yusof *et al.* 2016; Yamashita & Ando 2019) and nano-chemistry

† Email address for correspondence: ulisses@ciencias.unam.mx
‡ U.J.G.-H. and H.R. contributed equally to this work.

(Sesis *et al.* 2013). In the case of microscopic and submicroscopic applications, controlling the size of the bubbles is important (Xu *et al.* 2015; Fu *et al.* 2020). In general, the maximum size of a cavitation bubble is proportional to its lifetime (or oscillation time) (Rayleigh 1917), so that smaller bubbles require shorter oscillation times and thus higher driving frequencies.

In particular, inertial acoustic cavitation (i.e. an explosive bubble expansion due to the tension exceeding the cavitation nucleation threshold followed by the bubble's collapse) at high frequencies is difficult to achieve for two reasons. First, since the time available to a bubble to expand to a significant size is inversely proportional to the driving frequency, the driving forces expanding the bubble must be larger for higher frequencies (Brotchie, Grieser & Ashokkumar 2009). Second, the acoustic waves become strongly attenuated at high frequencies (Strohm & Kolios 2011), thereby making it difficult to reach the amplitude required to drive the bubble expansion. This is why controlled acoustic cavitation has not exceeded MHz frequencies (Wilson *et al.* 2019), with bubble lifetimes of a few microseconds, while bubbles nucleated in a substrate have longer lifetimes exceeding tens of microseconds (Bremond *et al.* 2005, 2006; Borkent *et al.* 2009; Yeo & Friend 2009).

Cavitation has also been produced via surface acoustic waves (SAWs; Rapet, Quinto-Su & Ohl 2020), also known as Rayleigh waves, which propagate along the surface of an elastic material (Rayleigh 1886). Their amplitude decays exponentially with the distance from the surface (depth), and most of the energy carried by the wave is concentrated in just one wavelength below the surface. So far, the highest frequency attained for cavitation bubbles is approximately 30–40 MHz (lifetimes (27 ± 3) ns; Pfeiffer *et al.* 2022); it required a combination of localised heating and a Lamb wave propagating in a very thin liquid gap. In the work of Rosselló & Ohl (2021, 2023), the on-demand production of bulk nano-bubbles through the passage of an intense laser pulse in water was demonstrated. Transient bubbles appear within the region exposed to light once a rarefaction wave passes through, attaining temporal and spatial control of the bulk nano-bubble nucleation.

In this work, we have achieved controlled inertial nano-bubble cavitation with continuously adjustable lifetimes in the range between 6 ns and 80 ns (oscillation frequencies in the range between 13 MHz and 166 MHz), nucleated at a nano-sized fracture on a glass substrate. Control is attained with a transient rarefaction wave, induced by the passage of a leaky Rayleigh wave on the glass surface. The tensile pressure explosively expands the nano-bubbles, which are later collapsed by the trailing shock wave in the liquid. Both pressure excitations are generated by a single laser pulse.

The process of the nano-bubble nucleation and collapse is illustrated in figure 1(*a*), where a laser pulse is focused in the vicinity of the nano-crack, generating a cavitation bubble and a Rayleigh wave in the substrate, followed by a slower shock wave in the liquid. Figure 1(*b*) depicts the sequence of events (1)–(5) close to the nucleation site (1). The second frame represents the time of arrival of the Rayleigh wave on the solid surface, leading to a tension state (2) in the liquid (positive stress in the glass that 'opens' the crack). The induced tension is strong enough to nucleate nano-bubbles at the nano-crack, the uneven structure of which acts as a cavitation nucleation site (3). The enduring negative pressure state in the liquid, induced by the passage of the SAW, keeps expanding the nucleated nano-bubbles (4) until the shock wave induces the collapse of the bubbles (5). The experiments are complemented with finite-volume (FV) simulations, showing excellent agreement.
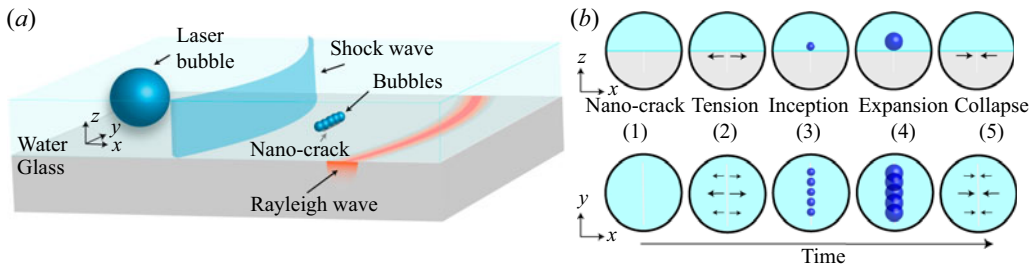
Figure 1. Inertial cavitation process. (*a*) A schematic of the sample, showing the Rayleigh and shock waves. The Rayleigh wave travels faster in the elastic solid than the shock wave in the liquid, and thus arrives first at the position of the nano-crack. (*b*) Close-up at the nano-crack position: (1) unperturbed nano-crack, (2) tension induced by the Rayleigh wave, (3) cavitation inception due to the tensile pressure, (4) bubble expansion due to ongoing tensile pressure, (5) bubble collapse induced by the arrival of the shock wave.
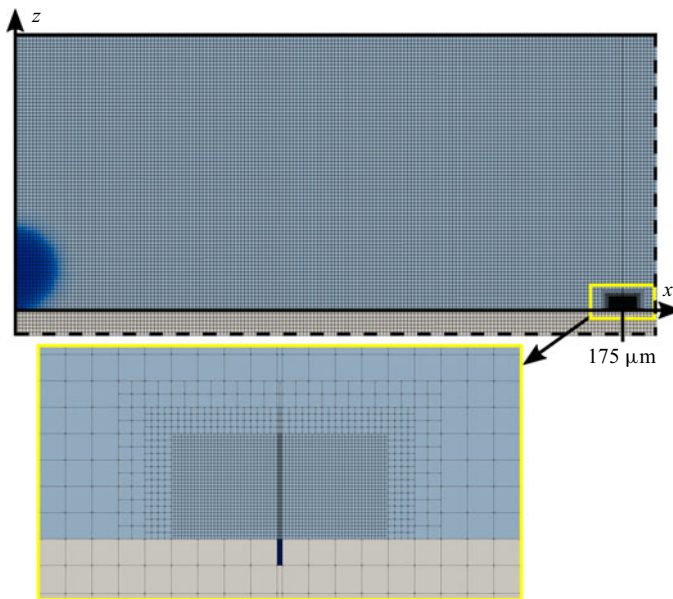

Figure 2. Computational mesh used for one of the axisymmetric FV simulations. The liquid is shown in light blue, the gas in dark blue, and the solid in light grey. A cylindrical fluid domain with height 80 μm and radius 1 mm sits on top of a solid domain with height 160 μm (not fully shown), which in turn sits on a gas-filled domain with height 80 μm (not shown). A cylindrical ring-shaped gas-filled defect is defined at $x = 175$ μm, with depth 1 μm and width 200 nm. The mesh is refined near the defect. A bubble is initiated on the axis of symmetry (z) with radius 12 μm.

2. Methods

2.1. *Experimental set-up*

The experimental set-up is based on our previous work (Gutiérrez-Hernández *et al.* 2021) where a laser pulse (6 ns, $\lambda = 532$ nm, SOLO PIV NewWave Research) is focused at the bottom of a thin liquid gap. The liquid (Epson printer ink, T6643 Magenta) is bounded by two borosilicate glass substrates, a microscope slide of thickness 1 mm, and a coverslip at the bottom of thickness 160 μm. The mechanical properties of the substrates are provided by the manufacturer (Fisherbrand, https://www.fishersci.es): elastic modulus $E = 63$ GPa, Poisson ratio $\nu = 0.2$, and density $\rho = 2230$ kg m^{-3}. The height of the

liquid is determined by spacers (≈ 80 µm). The sample is mounted on a motorised *x–y* stage. The laser beam is focused on a single spot above the lower substrate, with radius 12 µm and energy (200 ± 4) µJ. The linear absorption of the focused laser pulse causes the liquid to vaporise, and shock waves are emitted due to the sudden local increase of pressure (Lyamshev 1981). In the work of Quinto-Su, Suzuki & Ohl (2014), it has been shown that, for laser-induced micro-bubbles similar to those presented here, the rise in temperature is rather small with only a few Kelvin and decays quickly.

Since the laser is focused near the lower substrate, the sudden expansion of the bubble transfers energy to it almost instantaneously. This induces elastic deformation, transmitted as a bulk wave and a SAW, also known as a Rayleigh wave. In its propagation over the solid surface, the SAW also causes pressure changes in the liquid, inducing tensile pressures near the solid surface, i.e. the passage of the Rayleigh wave on the fluid–structure interface induces a rarefaction in the former.

We use a nano-crack in the glass at a lateral distance *d* from the position at which the laser bubble is generated, oriented orthogonally to the distance vector *d*. The nano-crack is generated by convergent shock waves (Gutiérrez-Hernández *et al.* 2022, 2023), and has width less than 100 nm. The distance *d* between the laser bubble and the nano-crack is controlled using the motorised stage.

The events are imaged with a CCD camera (Sensicam QE, PCO) and illuminated stroboscopically by a 6 ns laser pulse ($\lambda = 690$ nm, Orion, NewWave Research) at different delay times. Streak images are taken with a streak camera (SC-10, Optronis) and a 1 µs laser pulse ($\lambda = 637$ nm, L637G1 Thorlabs). Both red light sources are transmitted through a dichroic mirror of an inverted microscope.

2.2. *Numerical model*

Finite-volume simulations are carried out using the FluidStructureInteraction (FSI) package (OpenCFD Ltd 2016*a*) of the CFD software OpenFOAM (OpenCFD Ltd 2016*b*). The numerical solver CAVBUBBLEFSIFOAM is employed, which can model two compressible, immiscible fluids coupled with a deformable linear elastic solid. It has been used in previous works to model Rayleigh and shock waves in a thin liquid domain between two glass plates, obtaining good agreement with experimental observations (Gutiérrez-Hernández *et al.* 2022; Pfeiffer *et al.* 2022). The borosilicate glass with Young's modulus $E = 63$ GPa, density $\rho = 2230$ kg m^{-3} and Poisson's ratio $\nu = 0.2$ is modelled as a linear elastic solid, and solved for by the solver UNSTOTALLAGRANGIANSOLID. The linear elastic equation of motion is

$$\frac{\partial^2 \rho \boldsymbol{D}}{\partial t^2} - \nabla \cdot \left[G \nabla \boldsymbol{D} + G(\nabla \boldsymbol{D})^{\mathrm{T}} + \lambda \operatorname{tr}(\nabla \boldsymbol{D}) \mathbb{1} \right] = 0, \tag{2.1}$$

where $\boldsymbol{D}$ is the deformation, given in the solid's internal coordinates, $\mathbb{1}$ is the unity matrix, and

$$\lambda = \frac{\nu}{1 - 2\nu} \frac{1}{1 + \nu} E, \quad G = \frac{1}{2} \frac{1}{1 + \nu} E \tag{2.2a,b}$$

are the Lamé parameters.

The Newtonian fluids are modelled by the law of conservation of momentum

$$\rho \frac{\mathrm{D}\boldsymbol{u}}{\mathrm{D}t} = \rho \boldsymbol{f} - \nabla p + \mu \left(\Delta \boldsymbol{u} + \frac{1}{3} \nabla (\nabla \cdot \boldsymbol{u}) \right), \tag{2.3}$$

as well as the continuity equation

$$\frac{\partial \rho}{\partial t} + \nabla \cdot (\rho \boldsymbol{u}) = 0. \tag{2.4}$$

Gravitational effects are neglected.

The fluids represent a bubble filled with a non-condensable gas in water satisfying the Tait equation of state

$$p = (p_0 + B) \left(\frac{\rho}{\rho_0}\right)^{\gamma} - B, \tag{2.5}$$

with the values $p_0 = 101\,325$ Pa, $\rho_0 = 998.2061$ kg m^{-3}, $\gamma = 7.15$, $B = 303.6$ MPa for water, and $p_0 = 10\,320$ Pa, $\rho_0 = 0.12$ kg m^{-3}, $\gamma = 1.33$, $B = 0$ for the gas (which turns the equation of state into the ideal adiabatic gas equation). Here, p_0, ρ_0 is a known pair of values for the pressure and the density of a fluid. For water, γ and B are empirical parameters describing its low compressibility. For an ideal adiabatic gas with $B = 0$, γ becomes the adiabatic exponent. All changes of state are thus treated as adiabatic, and heat transfer is neglected.

The interface is captured using a phase fraction field α with interface compression to counteract numerical diffusion. Phase transitions and mass transfer between the fluid components are not modelled. Due to numerical inaccuracies, the mass of each fluid component is not exactly conserved, which is why in every time step, the bubble mass is corrected to stay constant over time.

The fluid–structure interaction is modelled using two-way coupling, where the elastic solid is acted upon by the fluids via surface forces $FS_i = \sigma \cdot \boldsymbol{n_i}$ that are given by the stress tensor in the fluid, $\sigma = -p\mathbb{1} + \mu[\nabla \otimes \boldsymbol{u} + (\nabla \otimes \boldsymbol{u})^{\mathrm{T}}]$. The solid acts on the fluid–structure interface by imposing its deformation $\boldsymbol{D}$ and velocity $\dot{\boldsymbol{D}}$ onto the boundary of the fluid domain. The solid and fluid equations of motion are solved alternately, either until a residual value characterising the discrepancy between the solid and fluid domains falls below a tolerance value, or for at most 100 iterations.

The numerical schemes used, such as the first-order upwind scheme, are at least of the order of accuracy 1.

The simulated geometry, as in the experiment, describes a thin sheet of water (height 80 µm) between a rigid upper boundary and an elastic glass sheet (height 160 µm). A defect in the shape of a cylindrical ring with height 1 µm and radial thickness 200 nm is inserted at the surface of the glass sheet. Since phase changes and thus cavitation processes are not modelled, it is filled with a gas that represents either trapped gas or a cavity created by the opening of the nano-crack in the experiment, and acts as a cavitation bubble nucleus. As in the experiment, a gas-filled domain of height 80 µm is added on the opposite side of the glass plate, allowing it to move away from or towards the water-filled domain. The outer boundaries as well as the bottom of the gas-filled domain below the solid plate are modelled as open, wave-transmissive boundaries. Because the geometry is chosen to be axisymmetric, it becomes effectively a two-dimensional problem, and only a thin wedge of a cylinder with radius 1 mm has to be modelled.

On the axis of symmetry of the domain, a spherical bubble with radius 12 µm and pressure 1.69 GPa is initiated. The initial condition for the pressure is consistent with previous works (Veysset *et al.* 2018; Gutiérrez-Hernández *et al.* 2021, 2022). It is based on the assumption that the energy deposition by the laser pulse happens on a much smaller time scale than the expansion of the created bubble, and it is thus assumed that

its initial density is equal to the density of the surrounding liquid. The initial radius is chosen such that the shock wave position over time matches closely that observed in the experiments. Since the shock wave velocity depends on its amplitude (the wave is faster in a denser medium), this is an indirect validation of the pressure amplitudes obtained in the simulations. Its vertical position is chosen to be equal to its radius, such that the lower end of the bubble touches the glass plate. To smoothen the surface of the bubble seed, it is smeared by applying the equation $\alpha' - 4 \times 10^{-11} \Delta \alpha' = \alpha$ to the phase fraction field α. The geometry is discretised into cells with width 10 μm in the gaseous domain below the glass plate, and 1 μm in most of the solid and the liquid domains (see figure 2). Near the crack, it is refined to width 125 nm. Since the crack is thinner than the 1 μm mesh before refinement, the cells above and below it are five times thinner than the surrounding cells.

2.3. *Modified Rayleigh–Plesset equation*

To describe the dynamics of a spherical bubble, including the compressibility of the liquid, we consider the modified Rayleigh–Plesset equation (Barber *et al.* 1997; Brenner, Hilgenfeldt & Lohse 2002; Vignoli *et al.* 2013)

$$\rho \left(R \ddot{R} + \frac{3}{2} \dot{R}^2 \right) = p_g(t) - p_0 - P(t) - 4\mu \frac{\dot{R}}{R} - \frac{2S}{R} + \frac{R}{c} \frac{\mathrm{d}p_g}{\mathrm{d}t}, \tag{2.6}$$

where $R = R(t)$ is the radius of the bubble, $\dot{R} = \mathrm{d}R/\mathrm{d}t$, p_g is the gas pressure inside the bubble, p_0 (= 101 325 MPa) is the pressure in the liquid far away from the bubble, $S = 72.8$ mN m^{-1} is the liquid surface tension, $\mu = 1$ mPa s is the dynamic viscosity of water, $P(t)$ is the driving pressure at the location of the bubble, and $c = 1500$ m s^{-1} is the speed of sound in the liquid. Considering the process as adiabatic, we use the van der Waals equation of state to describe the gas pressure inside the bubble:

$$p_g(t) = \left(P_0 + \frac{2S}{R_i} \right) \left(\frac{R_i^3 - h^3}{R^3(t) - h^3} \right)^\gamma, \tag{2.7}$$

where R_i is the initial radius, $\gamma = 4/3$ is the adiabatic index of water vapour, and $h = R_i/8.86$ is the characteristic van der Waals hard-core radius of the gas inside the bubble (Toegel *et al.* 2000). The external pressure $P(t)$ is obtained from the FV simulation without a defect in the glass and without any bubble besides the wave source in the centre of the domain. We extract the pressure from the fluid just above the solid as a function of time, $P(t)$, at different distances d. Then $P(t)$ for a given d is used in the modified Rayleigh–Plesset equation as the external driving pressure. The initial conditions are $\dot{R}(0) = 0$ and $R(0) = R_i$. Although this modified Rayleigh–Plesset model models a spherical bubble and does not consider complex interactions such as bubble–bubble interaction or proximity to solid surfaces, it is sufficient to understand and explain the cavitation process in this work.

3. Results and discussion

3.1. *Bubble formation and collapse*

Figure 3(*a*) shows a direct comparison between the strobe photographs taken in the experiment and simulation frames with a nano-crack placed at a lateral distance $d = 175$ μm from the centre of the laser bubble.
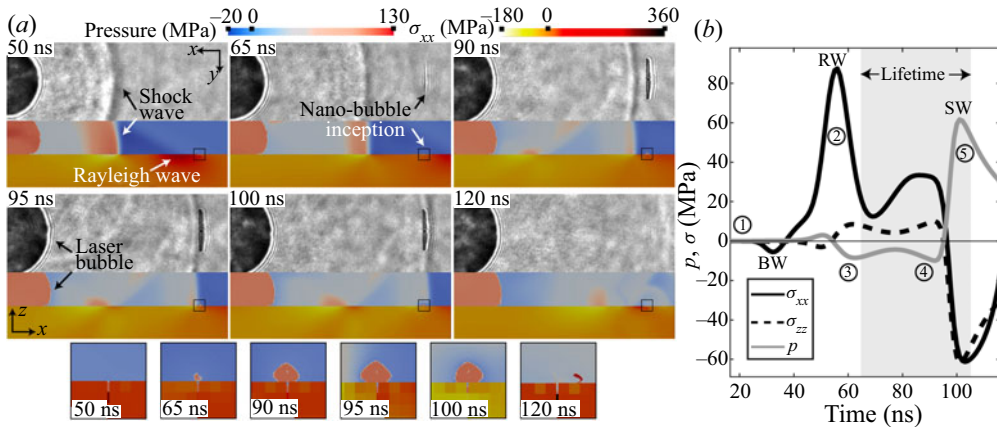
Figure 3. (*a*) Wave dynamics and nano-bubble nucleation. The first row shows strobe photographs (*x*–*y* plane), while the second row shows frames extracted from an FV simulation (*x*–*z* plane, where *z* is the axis of symmetry). The size of each strobe photograph is 200 µm × 70 µm. The simulation frames show the fluid in the top and the glass in the bottom half. The size of each simulation frame is 200 µm × 60 µm. The zoomed square frames (7 µm × 7 µm) on the bottom show a section of each frame centred at the fracture position in the simulation. Colour bars represent (*a*) pressure and (*b*) σ_{xx}, both in MPa. In the fluid, negative values indicate tensile pressure. In the solid, the positive and negative values of the σ_{xx} stress component mean tensile and compressive stress, respectively. (*b*) Simulated σ_{xx} and σ_{zz} stress components and pressure at the fluid–structure interface ($z = 0$) for a fracture at $d = 175$ µm. The arrival of the different waves is labelled at their respective peaks: bulk wave (BW), Rayleigh wave (RW) and shock wave (SW). The shaded region represents the time period in which the bubbles are visualised (strobe experiment). The stages marked in figure 1 are indicated here as circled numbers.

   The top half of each frame shows strobe photographs (*x*–*y* plane) of the events produced by the generation of the laser bubble at the sample. The strobe photographs are cropped (*x*–*y* plane, *x* > 0) to have a better comparison with the simulation. The dark semicircle on the left in the strobe photographs is the expanding laser-induced cavitation bubble, while the thinner dark curve propagating to the right is the shock wave. The bottom half of each frame shows FV simulation results of the same time as the photograph in a cross-section of the *x*–*z* plane, where *z* is the axis of symmetry and is located on the left border of the frame. The glass boundary is initially at $z = 0$, at half the height of the frame. The upper half of the simulated frame contains the liquid, where we observe the initial bubble and the shock wave ($\approx$1800 m s^{-1}). In the solid at the bottom half of the simulated frame, we can observe surface waves. In the first frame (50 ns), only the bulk wave ($\approx$5100 m s^{-1}, not shown) has reached the fracture position. In the frame at 65 ns, the Rayleigh wave ($\approx$3150 m s^{-1}) has passed (on the solid surface), and the tension region trailing behind it (in the liquid) causes the formation of nano-sized cavitation bubbles at the nano-crack. In the simulation, the tension causes the gas in the surface defect to begin to expand. In the next frames, the nano-bubbles continue to expand, until the shock wave passes through the position and collapses the bubbles, as we can see in the frames for 100 ns and 120 ns. We find excellent agreement between the FV simulations and the experiments. On the bottom, we show close-ups of the black squares drawn in the simulation frames. There, we can see in detail the behaviour of the gas in the cavity that emulates the nano-crack in the experiment. The Rayleigh waves that propagate on the solid are not visible in the experiment, likely because the deformation and density variations are so small that the change in the index of refraction is too small to overcome the noise of the image.

The calculated σ_{xx} (continuous black line) and σ_{zz} (dashed black line) stress components in the solid surface, and pressure in the liquid (continuous grey line), are extracted from the FV simulation and plotted in figure 3(*b*) for a case in which the laser pulse is focused at distance $d = 175$ µm from the nano-crack. There, the steps (1)–(5) of figure 1 are labelled. In the fluid, negative values indicate tensile pressure. In the solid, positive values of the stress components mean tensile stress, while negative values indicate compressive stress.

Initially, the nano-crack position ($d = 175$ µm) is undisturbed (1). Then, the bulk wave (BW) in the solid, which is the fastest wave excitation, arrives at 33 ns and is detected as a small negative (compressive) peak of the σ_{xx} stress component (-5.44 MPa). It is followed by the Rayleigh wave (RW) on the surface of the solid, which creates a large positive (tensile) peak of the σ_{xx} stress component, starting at 37 ns and reaching its maximum (87.5 MPa) at 56 ns (2). Meanwhile, the pressure in the liquid and the σ_{zz} stress component in the solid surface mirror each other. The σ_{zz} stress component has a small negative (compressive) peak (-3 MPa) at 50 ns followed by a positive (tensile) stress region that remains a few tens of nanoseconds, ending at 95 ns. On the other hand, in the liquid, the pressure has a small positive (compressive) peak (3 MPa), followed by a negative (tensile) pressure region. Two local minima are observed: -8.5 MPa at 62 ns (3), and -9.94 MPa at 92 ns. The pressure remains negative until the arrival of the shock wave (SW) in the liquid (5). This wave induces a pressure peak in the liquid of 61.6 MPa at 101 ns. In the solid surface, the shock wave induces strong compressive stresses, in both the σ_{xx} and σ_{zz} stress components, -61.24 MPa at 103 ns, and -61 MPa at 101 ns, respectively. The movies in the supplementary material available at https://doi.org/10.1017/jfm.2023.696, extracted from the simulations, show the expansion and collapse of the nano-bubbles at the fracture position for distances $d = 30, 40, 50, 75, 125, 175$ and 235 µm. A simulation is performed for each position of the fracture.

3.2. *Control of the bubble lifetime*

The time delay between the arrival of the Rayleigh wave and the shock wave is approximately proportional to their travelling time and the difference between their velocities. Hence by adjusting the lateral distance d between the laser focus and the nano-crack, we can control the lifetime of the nano-bubbles. To observe these extremely fast cavitation events in a single shot, we use a streak camera, which sweeps a one-dimensional image along a slit. The streak camera outputs a two-dimensional image (see figure 4*a*), where the vertical dimension is the slit and the horizontal dimension is time. The shock wave is seen as a shadow that propagates at speed 1800 m s^{-1} (SW, slope of the dashed red line). The laser-induced cavitation bubble is centred on the horizontal dashed white line and appears dark. The dashed blue line is the predicted position of the Rayleigh wave (RW, 3150 m s^{-1}) which is not captured. The bulk wave (BW) travelling at speed 5100 m s^{-1}, is also not captured. In comparison with the wave propagation dynamics, the expansion of the laser-induced bubble is relatively slow (200 m s^{-1}). A few nanoseconds after the Rayleigh wave reaches the position of the nano-crack ($d = 175$ µm), one or multiple bubbles are nucleated and expand for several tens of nanoseconds until the shock wave arrives, which induces their collapse. The lifetime of the nano-bubbles is the horizontal dimension denoted as LF. The section of the lifetime after the shock wave has passed is denoted as the collapse time t_{col}.

Figure 4(*b*) shows the superposition of 21 streak images, each with a different distance d between the nano-crack and the laser-induced bubble. We observe that the lifetime
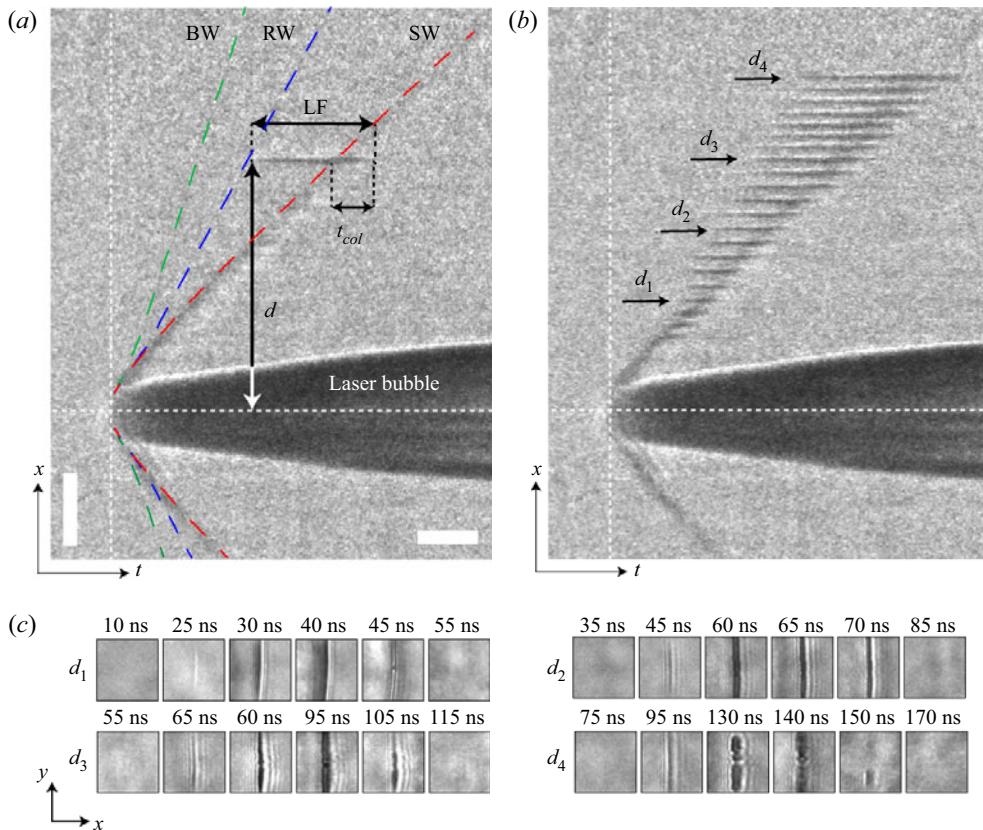
Figure 4. Control of the bubble lifetime. (*a*) Streak image for $d = 175$ μm. The vertical scale bar height (spatial) is 50 μm; the horizontal scale bar width (time) is 25 ns. The red, blue and green lines represent the shock, Rayleigh and bulk waves extracted from the simulations, respectively. (*b*) Superposition of the streak images for different positions *d*. (*c*) Strobe images of the nano-crack and cavitation bubbles for four distances: $d_1 = 75$ μm, $d_2 = 125$ μm, $d_3 = 175$ μm and $d_4 = 235$ μm. The size of each strobe photograph is 30 μm × 30 μm (*x–y* plane).

increases monotonically with *d*. In particular, we highlight four distances, $d_1 = 75$ μm, $d_2 = 125$ μm, $d_3 = 225$ μm and $d_4 = 235$ μm, at which we also performed experiments with stroboscopic illumination in order to image the nano-bubbles in the *x–y* plane. Selected frames at different time delays are shown in figure 4(*c*).

In figure 5, the measured lifetime is plotted as a function of the lateral distance *d* between the laser focus and the nano-crack. The black square symbols are the measurements from the streak camera for 21 distances. The error bars represent the standard deviation over 40 repetitions. The streak images are analysed considering the light intensity at each position in order to differentiate the bubble from the background.

The largest distance at which we observed a bubble is $d = 235$ μm, with lifetime (71 ± 6) ns. A decrease in the lifetime is observed as *d* gets smaller. The smallest distance at which a bubble is observed is $d = 50$ μm. For this distance, we measured a lifetime (9 ± 3) ns. A further decrease of *d* is expected to result in even smaller lifetimes, but because of the large values of the stress components, a modification in the fracture on the glass surface was observed, so the conditions were modified in each shot.
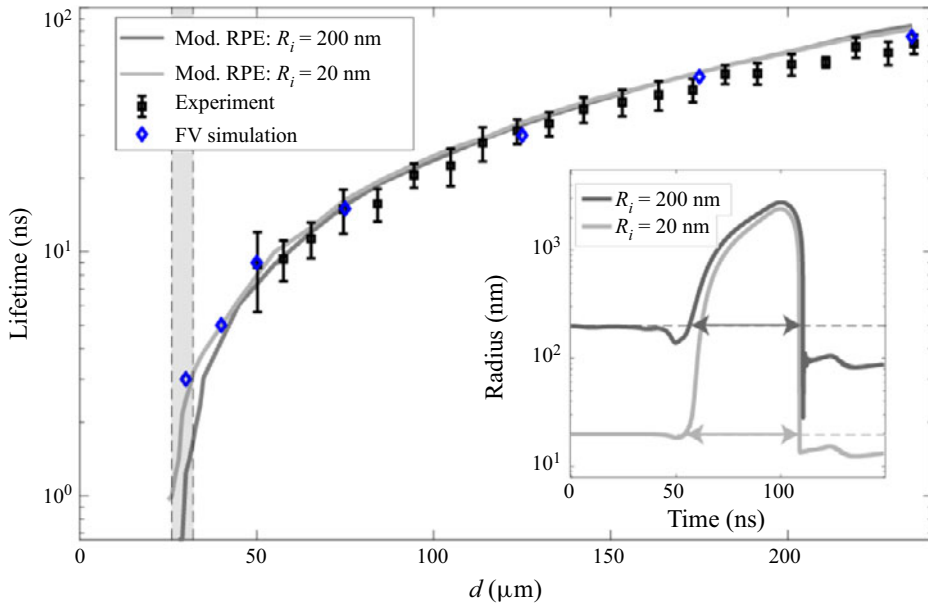
Figure 5. Bubble lifetime as a function of d. The black symbols represent the lifetime measured from the streak experiments for 21 distances. The error bars represent the standard deviation over 40 repetitions. The blue symbols indicate the lifetime extracted from the FV simulations. The continuous lines represent the lifetime extracted from the solution of the modified Rayleigh–Plesset equation (mod. RPE) using two different initial radii: 200 nm (grey) and 20 nm (light grey). The dashed vertical line at 26 µm indicates the smallest distance d at which there is no bubble expansion in the modified Rayleigh–Plesset equation, while the dashed vertical line at 32 µm indicates the smallest distance d at which the bubble surpasses 10 times its initial radius. Inset: Rayleigh–Plesset equation solution. Radius as a function of time for $R_i = 20$ nm and $R_i = 200$ nm (shown as horizontal dashed lines) at $d = 175$ µm. The arrows denote the bubble's lifetime. The external pressure as a function of time is extracted from the FV simulation (figure 3b).

To get a better understanding of the nano-bubble dynamics, we use the modified Rayleigh–Plesset equation (Barber *et al.* 1997; Brenner *et al.* 2002) that describes the bubble dynamics $R(t)$ and considers the effects of the compressibility of the liquid (2.6).

The external pressure $P(t)$ is obtained from the FV simulation without a defect in the glass. In this way, we extract the pressure $P(t)$ in the liquid just above the solid surface as a function of time at different distances d. The equation is solved for R_i in the range 10–1000 nm. In order to make an estimation of a realistic initial bubble radius R_i, we consider the spatial resolution, which yields 600 nm px^{-1}. Hence we do not resolve the initial stages of bubble expansion, but we can still detect the change in the transmitted light intensity as the bubbles expand.

Since the initial bubble is invisible, we can assume that $R_i < 300$ nm. Furthermore, we find that a bubble with $R_i = 10$ nm ceases to expand for larger distances ($d > 175$ µm), since there the magnitude of the negative pressure does not reach the Blake threshold. This is explained in detail in § 3.2.2. Hence we consider R_i in the range between 20 and 200 nm. In this range, the maximum bubble radius and bubble lifetime are fairly insensitive to R_i.

The results for the calculated lifetimes as a function of d are plotted in figure 5 as continuous lines. The inset is a plot of the nano-bubble dynamics $R(t)$ for $R_i = 20$ nm (light grey) and $R_i = 200$ nm (grey) at $d = 175$ µm. For each case, the arrow denotes the bubble's lifetime. Since the bubble first experiences a small compression due to the moderate over-pressure in the liquid, the measurement starts once the bubble exceeds its

972 A16-10

initial size, and ends once it is again smaller than the initial radius. Figure 5 also shows two vertical lines: the line at 26 μm indicates the smallest distance at which there is no bubble expansion, while the line at 32 μm indicates the smallest distance at which the bubble with $R_i = 20$ nm surpasses 10 times its initial radius.

The lifetimes extracted from the FV simulation are plotted as blue diamonds, which show a trend similar to that of the measurements, including the absence of bubbles for $d \leq 26$ μm. At those distances, the pressure in the liquid does not reach negative values due to the lack of separation between the Rayleigh wave and the shock wave. Hence, for such a small d, the nano-bubbles do not expand regardless of their initial size. For $d = 30$ μm, the lifetime obtained from the simulation is only 3 ns.

The results obtained from the experimental observations, the FV simulations and the modified Rayleigh–Plesset equation are in excellent agreement for smaller d, with the modified Rayleigh–Plesset equation slightly overestimating the lifetimes for larger d.

3.2.1. *Initial radius*
The radius evolution predicted by the modified Rayleigh–Plesset equation (2.6) for $d = 175$ μm and several initial radii R_i is plotted in logarithmic scale in figure 6(*a*). The driving pressure used is shown in figure 3(*b*). For $R_i = 8$ nm, we observe a significant expansion of the bubble at approximately $t = 90$ ns. Nevertheless, the maximum radius reached is below 200 nm. For smaller initial radii R_i, the expansion is even smaller. For R_i in the range from 10 nm to 1 μm, the dynamics, lifetimes and maximum radii are similar. The expansion starts at $\approx$57 ns, and the maximum radius is attained at $\approx$100 ns. Hence the experimentally observable dynamics is only weakly sensitive to the initial condition of the simulated bubble. For $R_i = 10$ nm, the maximum radius is 2.14 μm at 99 ns, i.e. an expansion of 214 times its initial size. For $R_i = 200$ nm, the maximum radius is 2.74 μm at 100 ns, i.e. $\sim$14 times larger. This expansion factor becomes smaller for larger initial radii. The maximum bubble expansion R_{max} seemingly approaches an upper limit of approximately 3 μm. For $R_i > 200$ nm, we observe weak volume oscillations after the collapse.

3.2.2. *Blake's limit*
If a bubble's surface tension force exceeds the external tension acting at its surface plus its internal gas pressure, then it does not expand. The critical bubble size R_C below which the bubble does not expand is given by Blake's limit (Brennen 2013)

$$P_{min} = p_v - \frac{4S}{3R_C}, \tag{3.1}$$

where P_{min} is the smallest external pressure (strongest tension), and p_v is the vapour pressure. The upper graph in figure 6(*b*) shows the minimum pressure extracted from the FV simulation without a defect as a function of the distance d from the wave source. The lower graph shows the critical radius R_C obtained with (3.1) using the values for P_{min} from the upper graph. We observe the first negative pressure at $d = 26$ μm, with corresponding critical radius approximately $R_C = 34$ nm. The strongest tension ($P_{min} = -43$ MPa) is found at $d = 46$ μm. Here, the critical radius is only $R_C = 3$ nm. As is expected, after the absolute minimum, the tension decays and the critical radius increases with increasing d. The dashed line indicates the distance $d = 175$ μm used for figure 6, where $R_C = 12$ nm for pressure $P_{min} = -8.5$ MPa. This threshold agrees with the limit $R_i = 10$ nm obtained from the modified Rayleigh–Plesset equation. The last distance for which bubbles are
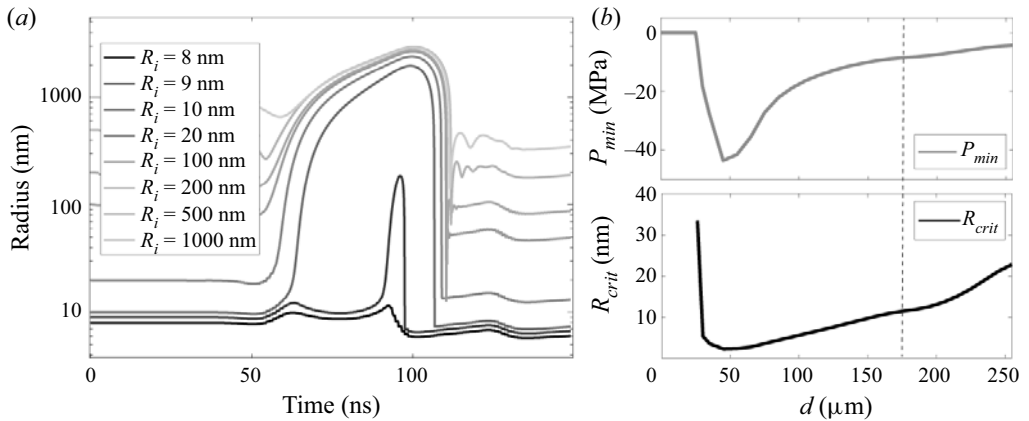
Figure 6. Solutions of the modified Rayleigh-Plesset equation with different initial radii R_i. (a) The external pressure used is for a bubble placed at distance $d = 175$ µm from the origin; $R_i = 8$ nm is the first radius at which a strong bubble expansion is seen ($R_{max} = 0.17$ µm). We observe an approach to a maximum radius ($R_{max} \approx 3$ µm) for bigger R_i. (b) The upper plot shows the extracted minimum pressure P_{min} as a function of the distance from the origin d is plotted. We observe the first negative pressure at $d = 26$ µm, an absolute minimum at 46 µm, and an approach to zero as d gets bigger. The lower plot shows the graph of the critical radius (R_C) obtained with (3.1), with the P_{min} values from the upper graph. The dashed line indicates $d = 175$ µm, where R_C is close to 10 nm for pressure -8.5 MPa.

observed is $d_4 = 235$ µm, where the maximum tensile pressure is -5.12 MPa, and the corresponding critical radius is 19 nm. It is important to point out that the impurities in the liquid sample could cause the cavitation threshold to be different from that of pure water.

Figure 7 shows the maximum bubble radius as a function of the distance d obtained from the solution of the modified Rayleigh–Plesset equation, with different initial radii R_i. For $R_i = 10$ nm at $d = 195$ µm, the maximum expansion R_{max} is significantly smaller compared to that for larger R_i. This is explained by Blake's limit. The minimum pressure at this distance is -7.74 MPa, and the critical radius is 12.5 nm. Although an expansion is observed, it does not exceed 600 nm. The vertical dashed line at 26 µm indicates the distance at which no tensile pressure occurs.

4. Conclusion

We demonstrate a novel approach to nucleate cavitation bubbles on a surface at a precise location on previously deposited nanometre-sized inhomogeneities. The expansion is driven by a leaky Rayleigh wave that propagates on the surface of the glass, while the inertial collapse is induced by a trailing shock wave that propagates in the liquid. Both waves are generated by a single laser pulse. We show experimentally that the bubble lifetimes can be controlled by varying the distance of wave propagation. For the largest distance studied, the measured lifetime is (71 ± 6) ns, while for the smallest distance, the measured lifetime is (9 ± 3) ns.

We find good agreement between the experimental results and those obtained from the finite-volume simulations and the modified Rayleigh–Plesset equation. Although the latter is a rather simple model valid only for a single spherical bubble, in which neither bubble–bubble interaction nor its interaction with a nearby solid wall is considered, it shows excellent agreement with the experimental and finite-volume simulation results
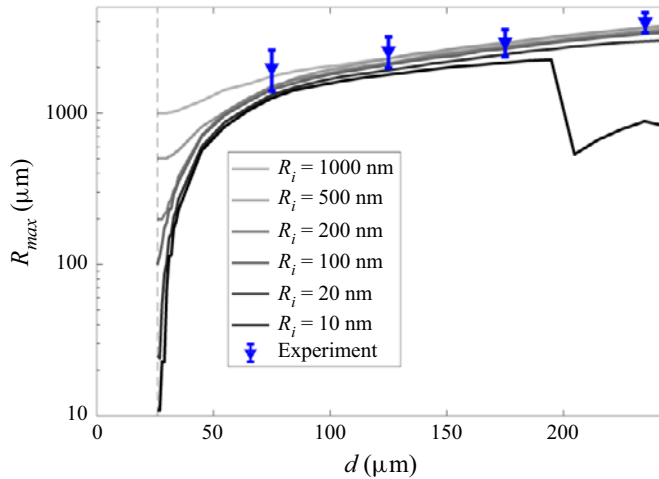
Figure 7. Maximum radius as a function of the distance d. The solid lines are the maximum radius plotted at each position, obtained from the solutions of the modified Rayleigh–Plesset equation. Each curve has different initial conditions for R_i. The vertical dashed line at 26 µm indicates the smallest distance at which we observe bubble expansion, independently of the initial radius. At $d = 25$ µm, no negative pressure occurs. The blue symbols represent the maximum radius measured from the strobe experiments for the distances $d = 75$, 125, 225 and 235 µm.

in terms of the bubble lifetimes, and allows us to make a complete description of the expansion and collapse of the bubbles at various distances d from the wave source.

This new regime of ultra-high frequency inertial cavitation scales the well-known energy-focusing capability of cavitation bubbles from the micrometre world to the nano-world, still maintaining perfect and repeatable control over their dynamics in time and space.

In future works, by varying the geometry, we could explore even shorter bubble lifetimes. In a previous study, using a ring geometry for the laser-induced bubble and the emitted waves (Gutiérrez-Hernández *et al.* 2022), we show a time delay of only 7 ns between the convergence of a Rayleigh wave on the surface and a shock wave in the liquid. Therefore, we expect to study bubbles with lifetimes below 10 ns. The present work opens up novel perspectives in frameworks such as the detection of nano-fractures in surfaces using the expansion of nano-cavitation.

Supplementary movies. Supplementary movies are available at https://doi.org/10.1017/jfm.2023.696.

Declaration of interests. The authors report no conflict of interest.

Data availability statement. The data that support the findings of this study are available from the corresponding author upon reasonable request.

Author ORCIDs.

Ulisses J. Gutiérrez-Hernández https://orcid.org/0000-0001-6930-8546;

Hendrik Reese https://orcid.org/0000-0001-8622-1856;

🔟 Claus-Dieter Ohl https://orcid.org/0000-0001-5333-4723;

🔟 Pedro A. Quinto-Su https://orcid.org/0000-0002-8363-3932.

REFERENCES

BARBER, B.P., HILLER, R.A., LÖFSTEDT, R., PUTTERMAN, S.J. & WENINGER, K.R. 1997 Defining the unknowns of sonoluminescence. *Phys. Rep.* **281** (2), 65–143.

BORKENT, B.M., GEKLE, S., PROSPERETTI, A. & LOHSE, D. 2009 Nucleation threshold and deactivation mechanisms of nanoscopic cavitation nuclei. *Phys. Fluids* **21** (10), 102003.

BREMOND, N., ARORA, M., OHL, C.-D. & LOHSE, D. 2005 Cavitation on surfaces. *J. Phys.: Condens. Matter* **17** (45), 102003.

BREMOND, N., ARORA, M., OHL, C.-D. & LOHSE, D. 2006 Controlled multibubble surface cavitation. *Phys. Rev. Lett.* **96**, 224501.

BRENNEN, C.E. 2013 *Cavitation and Bubble Dynamics*. Cambridge University Press.

BRENNER, M.P., HILGENFELDT, S. & LOHSE, D. 2002 Single-bubble sonoluminescence. *Rev. Mod. Phys.* **74**, 425–484.

BROTCHIE, A., GRIESER, F. & ASHOKKUMAR, M. 2009 Effect of power and frequency on bubble-size distributions in acoustic cavitation. *Phys. Rev. Lett.* **102**, 084302.

CHEN, H., KREIDER, W., BRAYMAN, A.A., BAILEY, M.R. & MATULA, T.J. 2011 Blood vessel deformations on microsecond time scales by ultrasonic cavitation. *Phys. Rev. Lett.* **106**, 034301.

FU, Y., LU, H., NIAN, G., WANG, P., LIN, N., HU, X., ZHOU, H., YU, H., QU, S. & YANG, W. 2020 Size-dependent inertial cavitation of soft materials. *J. Mech. Phys. Solids* **137**, 103859.

GUTIÉRREZ-HERNÁNDEZ, U.J., DE COLLE, F., OHL, C.-D. & QUINTO-SU, P.A. 2021 Transient time-delay focusing of shock waves in thin liquids. *J. Fluid Mech.* **910**, A27.

GUTIÉRREZ-HERNÁNDEZ, U.J., REESE, H., OHL, C.-D. & QUINTO-SU, P.A. 2022 Bullseye focusing of cylindrical waves at a liquid–solid interface. *Phys. Fluids* **34** (11), 112013.

GUTIÉRREZ-HERNÁNDEZ, U.J., REESE, H., REUTER, F., OHL, C.-D. & QUINTO-SU, P.A. 2023 Nano-cracks and glass carving from non-symmetrically converging shocks. *Adv. Phys. Res.* **2** (9), 2300030.

LYAMSHEV, L.M. 1981 Optoacoustic sources of sound. *Sov. Phys. Uspekhi* **24** (12), 977–995.

OPENCFD LTD 2016*a* *Fluid Structure Interaction*. ESI Group.

OPENCFD LTD 2016*b* *Foam-Extend-4.0*. ESI Group.

PFEIFFER, P., EISENER, J., REESE, H., LI, M., MA, X., SUN, C. & OHL, C.-D. 2022 Thermally assisted heterogeneous cavitation through gas supersaturation. *Phys. Rev. Lett.* **128**, 194501.

PRENTICE, P., CUSCHIERI, A., DHOLAKIA, K., PRAUSNITZ, M. & CAMPBELL, P. 2005 Membrane disruption by optically controlled microbubble cavitation. *Nat. Phys.* **1** (2), 107–110.

QUINTO-SU, P.A., SUZUKI, M. & OHL, C.-D. 2014 Fast temperature measurement following single laser-induced cavitation inside a microfluidic gap. *Sci. Rep.* **4**, 5445.

RAPET, J., QUINTO-SU, P.A. & OHL, C.-D. 2020 Cavitation inception from transverse waves in a thin liquid gap. *Phys. Rev. Appl.* **14** (2), 024041.

RAYLEIGH, LORD 1886 On waves propagated along the plane surface of an elastic solid. *Proc. Lond. Math. Soc.* **s1-17**, 4–11.

RAYLEIGH, LORD 1917 VIII. On the pressure developed in a liquid during the collapse of a spherical cavity. *Lond. Edinb. Dublin Philos. Mag. J. Sci.* **34** (200), 94–98.

ROSSELLÓ, J. & OHL, C.-D. 2021 On-demand bulk nanobubble generation through pulsed laser illumination. *Phys. Rev. Lett.* **127**, 044502.

ROSSELLÓ, J. & OHL, C.-D. 2023 Clean production and characterization of nanobubbles using laser energy deposition. *Ultrason. Sonochem.* **94**, 106321.

SESIS, A., HODNETT, M., MEMOLI, G., WAIN, A.J., JUREWICZ, I., DALTON, A.B., CAREY, J.D. & HINDS, G. 2013 Influence of acoustic cavitation on the controlled ultrasonic dispersion of carbon nanotubes. *J. Phys. Chem.* B **117** (48), 15141–15150.

STRIDE, E. & COUSSIOS, C. 2019 Nucleation, mapping and control of cavitation for drug delivery. *Nat. Rev. Phys.* **1** (8), 495–509.

STROHM, E.M. & KOLIOS, M.C. 2011 Sound velocity and attenuation measurements of perfluorocarbon liquids using photoacoustic methods. In *2011 IEEE International Ultrasonics Symposium, Orlando, FL, USA*, pp. 2368–2371. IEEE.

TOEGEL, R., GOMPF, B., PECHA, R. & LOHSE, D. 2000 Does water vapor prevent upscaling sonoluminescence? *Phys. Rev. Lett.* **85**, 3165–3168.

VEYSSET, D., GUTIÉRREZ-HERNÁNDEZ, U., DRESSELHAUS-COOPER, L., DE COLLE, F., KOOI, S., NELSON, K.A.A., QUINTO-SU, P.A.A. & PEZERIL, T. 2018 Single-bubble and multibubble cavitation in water triggered by laser-driven focusing shock waves. *Phys. Rev.* E **97** (5), 053112.

VIGNOLI, L.L., DE BARROS, A.L.F., THOMÉ, R.C.A., NOGUEIRA, A.L.M.A., PASCHOAL, R.C. & RODRIGUES, H. 2013 Modeling the dynamics of single-bubble sonoluminescence. *Eur. J. Phys.* **34** (3), 679–688.

WILSON, C.T., *et al*. 2019 Comparative study of the dynamics of laser and acoustically generated bubbles in viscoelastic media. *Phys. Rev.* E **99**, 043103.

XU, S., ZONG, Y., FENG, Y., LIU, R., LIU, X., HU, Y., HAN, S. & WAN, M. 2015 Dependence of pulsed focused ultrasound induced thrombolysis on duty cycle and cavitation bubble size distribution. *Ultrason. Sonochem.* **22**, 160–166.

YAMASHITA, T. & ANDO, K. 2019 Low-intensity ultrasound induced cavitation and streaming in oxygen-supersaturated water: role of cavitation bubbles as physical cleaning agents. *Ultrason. Sonochem.* **52**, 268–279.

YEO, L.Y. & FRIEND, J.R. 2009 Ultrafast microfluidics using surface acoustic waves. *Biomicrofluidics* **3** (1), 102003.

YUSOF, N.S.M., BABGI, B., ALGHAMDI, Y., AKSU, M., MADHAVAN, J. & ASHOKKUMAR, M. 2016 Physical and chemical effects of acoustic cavitation in selected ultrasonic cleaning applications. *Ultrason. Sonochem.* **29**, 568–576.